Nano-scale microstructure of Fe3+-, OH--bearing crystalline inclusions in experimentally oxidized olivine from a mantle nodule

5 authors, including:

Natalia R. Khisina
Russian Academy of Sciences
82 PUBLICATIONS   **378** CITATIONS

SEE PROFILE

Nano-scale microstructure of Fe^{3+}-, OH^--bearing crystalline inclusions in experimentally oxidized olivine from a mantle nodule

N. R. Khisina[1,*], K. Langer[2], M. Andrut[3], A. V. Ukhanov[1] and R. Wirth[4]

[1] Institute of Geochemistry and Analytical Chemistry, Russian Academy of Sciences, Kosygin st. 19, 117975 Moscow, Russia
[2] Institut für Angewandte Geowissenschaften, TU Berlin, Ernst-Reuter Pl. 1, D-10587 Berlin, Germany
[3] Institut für Petrologie, Universität Wien, Geozentrum, Althanstraße 14, A-1090 Wien, Austria
[4] GeoForschungsZentrum Potsdam, Telegrafenberg C-120, D-14473 Potsdam, Germany

ABSTRACT

An olivine grain from peridotite nodule 9206 (Udachnaya kimberlite) was heated in air at 700°C for 9 h. It was investigated by EMPA, by IR and UV spectroscopy and by TEM. The TEM examination reveals hexagon-like inclusions up to several hundred nm in size with a core and rim structure. The AEM data show that the inclusions contain only Mg, Fe and Si as cations. The rims have almost the same composition as the olivine matrix whereas the cores are enriched in iron and depleted in Mg. Electron diffraction data, SAED and CBED, indicate that the rims are composed of a 'secondary' olivine while the cores are composed of coexisting feroxyhite FeOOH, bernalite $Fe(OH)_3$ and β-cristobalite SiO_2. The presence of nm-sized inclusions in minerals is expected to influence the interpretation of spectroscopic results if spectroscopy is carried out without knowledge of the microstructure.

It is speculated that the complex microstructure of the inclusions is a result of a solid state transformation of a precursor phase, probably a hydrous magnesian silicate, during the experimental heating and oxidation.

KEYWORDS: olivine, laihunite, bernalite, electron diffraction, EELS, peridotite.

Introduction

Solid state reactions such as the oxidation and hydration (protonization) of olivine seem to be controlled by the creation, diffusion and segregation of point defects resulting in either planar defect formation or precipitation of new phase(s). Point defect characteristics control the replacement of olivine by iron oxides such as laihunite, humite-like minerals, serpentine and iddingsite during oxidation and hydration. Both the concentration of Fe^{3+} and/or OH^- incorporated into the olivine structure as well as the defect behaviour depend on temperature, pressure, P_{O_2} and P_{H_2O}. Therefore, the defects which are observed in natural olivines should retain a 'memory' of the conditions of formation and post-crystallization history of the sample.

During the last ten years, synthesis of dense hydrous Mg silicates (DHMS) under high-pressure–high-temperature conditions as well as the investigation of the water content in typically anhydrous silicates like olivine have been of great interest in mantle petrology. The DHMS are thought to be potential water-bearing minerals in subduction zones (Liu, 1987; Thompson, 1992; Burnley and Navrotsky, 1996; Prewitt et al., 1997; Kudoh et al., 1993).

Infrared spectroscopy is typically used to determine the water content of olivine. Olivines of different origin including mantle nodules have been investigated (Beran and Putnis, 1983; Freund and Oberheuser, 1986; Miller et al., 1987; Bai and Kohlstedt, 1993; Young et al.,

* E-mail: urusov@geol.msu.ru

1993; Kitamura *et al.*, 1987; Libowitsky and Beran, 1995). Very low water concentrations such as 0.04 ± 0.01 wt.% (Beran and Putnis, 1983), 0.002 wt.% (Bai and Kohlstedt, 1993) have been measured. Absorption bands observed in the OH^- valence vibrational region of the IR spectra of olivines were interpreted as OH^- point defects incorporated in the olivine structure, charge-compensated by cation vacancies in either M1 and/or M2 octahedra or in tetrahedral sites of Si (Libowitsky and Beran, 1995). In addition to such point defects, OH^--bearing planar defects or OH^--bearing phases may also be present and give rise to $v_{OH'}$. For instance, IR spectra of mantle olivine from kimberlite revealed typical OH absorption bands (Kitamura *et al.*, 1987) which can be interpreted in terms of OH^- point defects, whereas TEM investigations of the same sample showed the presence of OH-bearing planar defects (humite-like layers) (Kitamura *et al.*, 1987). Thus, IR studies must be combined with TEM as was the case in Kitamura *et al.* (1987) and Beran and Putnis (1983).

The defect structure of olivine is very sensitive to oxygen fugacity. The existence of Fe^{3+}-bearing defects depends not only on f_{O_2} but on the *P-T* conditions too. Beside the buffered reactions of olivine oxidation with formation of magnetite and/or hematite, a so called laihunitization process can proceed resulting in the formation of oriented planar defects of ferriolivine composition (Khisina *et al.*, 1995, 1998; Janney and Banfield, 1998; Dyar *et al.*, 1998). Laihunite, a new mineral with defect cation-deficient olivine-like structure and ideal chemical formula $Fe^{2+}_{0.5}Fe^{3+}_{1.0}SiO_4$, was discovered as a natural product of fayalite oxidation (Laihunite Research Group, 1976). Model experiments on powdered natural olivine at 1 atm showed that laihunite is formed as a metastable phase during early stages of olivine oxidation at high oxygen fugacity and low temperature (<750°C) (Khisina *et al.*, 1999). It was assumed that the boundary laihunite/magnetite in the P_{O_2}-T phase diagram should be shifted with increasing pressure towards higher temperatures thus expanding the laihunite field (Khisina *et al.*, 1999). In that case laihunite can be expected to occur in the mantle. This idea is supported by the finding of laihunite in a mantle nodule (Banfield *et al.*, 1992).

The aim of the heating experiment reported here is the investigation of the behaviour of OH^- and Fe^{3+} bearing defects in olivine under oxidizing conditions. A natural olivine sample from a mantle nodule in a kimberlite was used as the starting material. The sample was investigated by absorption spectroscopy in the infrared (IR) and ultraviolet (UV) spectral regions, electron microprobe analysis (EMPA) as well as transmission electron microscopy (TEM) including high resolution electron microscopy (HRTEM), analytical electron microscopy (AEM), selected area electron diffraction (SAED), convergent beam electron diffraction (CBED) and electron energy-loss spectroscopy (EELS).

Description of the nodule

Olivine from the small peridotite nodule 9206, sampled from the kimberlite pipe Udachnaya by A. Ukhanov, was used as the starting material for the experiments. This special peridotite is not typical of the xenoliths incorporated in the pipe. The nodule 9206 is similar in texture and mineral composition to the peridotites of the 'coarse-grained group' which are common xenoliths from the Obnajennaya pipe. Like these, nodule 9206 is characterized by a granoblastic texture and rounded grains. Most of the coarse-grained fragments of upper-mantle peridotite entrained in the kimberlite magma have disintegrated during intrusion and have loaded the melt with abundant grains of so-called 'first-generation olivine'.

Intergranular serpentine bands and veinlets penetrating the nodules indicate disintegration. The intensity of serpentinization is variable in the nodule 9206. In different thin sections small olivine relics embedded in a serpentine matrix as well as large areas of olivine separated by narrow serpentine veins can be observed. Pale-greenish lizardite is the predominant species of serpentine. Its fibres are oriented perpendicular to the olivine/lizardite phase boundaries. Serpophite (the isotropic variety of serpentine) occurs along cracks and is usually accompanied by tiny magnetite grains. Brucite occurs (locally) at contacts with olivine as thin colourless rims. In nodule 9206, minor orthopyroxene (opx) has been replaced completely by talc-chlorite pseudomorphs surrounded by dark magnetite-chlorite rims. However, rare scattered clinopyroxene (cpx) grains are almost unaffected by serpentinization. Cpx is typical for peridotite nodules and is characterized by low-Fe diopside with moderate contents of jadeite and kosmochlore. Serpentinization has no impact on accessory Cr-spinel, which shows a high Cr/(Cr+Al) ratio

(0.52) and low Fe^{3+}/Fe (0.185) and $Fe^{2+}/(Fe+Mg)$ (0.48) ratios, typical for spinel of harzburgite nodules (Matsyuk *et al.*, 1989).

Whole-rock analyses of the nodule 9206 (Table 1) shows that excluding these two components, nodule 9206 (closely) matches a 'depleted' dunite-harzburgite chemical composition. Undulatory extinction, patchy zones and other strain features in the olivine which are typical for most of the nodules are absent in nodule 9206. The *PT* conditions of formation of the 9206 nodule rock are considered to be 700–800°C and 5.5–6.0 GPa (Ukhanov *et al.*, 1988).

Experimental and analytical conditions

A single olivine grain (15 mm in size) from the nodule described above was heated for 9 h in air at 700°C. A plate (of thickness 119 μm) polished on both sides was prepared with the (100) plane as surface plane. This (100) plate was investigated by EMPA, IR spectroscopy and UV microscope spectrometry methods. Afterwards it was repolished and ion-beam thinned to electron transparency for the TEM investigation.

Unpolarized single crystal IR absorption spectra were measured by means of a Bruker IFS 66v FTIR spectrometer with attached microscope. The spectrometer was equipped with a globar light source, a KBr-beam splitter and MCT-detector. The IR absorption was recorded in the spectral range 4000 to 2600 cm^{-1} with a resolution of 2 cm^{-1}. The measuring spot was 32 mm in diameter. Spectra were averaged over 256 scans. Phase correction was performed following a procedure after Mertz (cf. Griffiths and de Haseth, 1986), and the Norton-Beer-weak mode was chosen as the apodization function. Locally resolved spectral measurements in the UV spectral range 34000–12500 cm^{-1} were scanned using a Zeiss UMSP 80 microscope spectrometer with a Glan-Thompson-type calcite polarizer and UV-transparent Ultrafluars (Zeiss) 10 × lens as objective and condenser. Transmission electron microscopy (TEM) and AEM were carried out at 200 kV in a Philips CM200 electron microscope, equipped with a LaB_6 electron source. Electron energy-loss spectroscopy EELS was performed with a Gatan $GIF^{®}$ imaging filter in the diffraction mode, camera length 50 mm, beam diameter 55 nm and condenser aperture 100 μm. Spectra were recorded with an energy dispersion of

0.3 eV/channel. The instrumental energy resolution measured at full width of half maximum (FWHM) of the zero-loss peak was 1.8 eV. Spectra were obtained by cumulative acquisition (10–15 spectra) with an acquisition time of 0.2–1 s to prevent irradiation damage. The AEM was performed at 200 kV in the scanning mode with an EDAX X-ray analyser with ultrathin window. The electron beam diameter was ~4 nm, and the total acquisition time was 60–100 s. Quantitative analyses have been carried out using a San Carlos olivine standard to determine the k_{AB} factors. The quantitative analyses are normalized to 100%. The relative error of the analyses depends mainly on the accumulated count rates. A minimum accumulated count rate was used to give a relative error of ~13%.
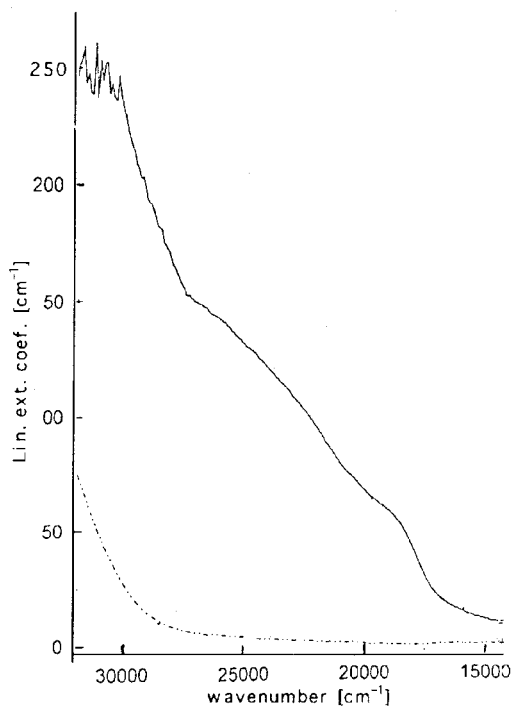

FIG. 1. Polarized UV/vis spectra of the oxidation rim (upper spectrum) and unoxidized interior (lower spectrum) of the olivine crystal; E//x//b. The spectrum of the oxidation rim exhibits shoulders at 19000 and 25000 cm^{-1} indicating the presence of Fe^{3+}-bearing phases.

TABLE 1. Bulk chemical composition and mineral composition of the nodule 9206 from the kimberlite pipe Udachnaya-East (Northen Yakutiya).

Oxide wt.%	Bulk rock comp. wt.%	Olivine wt.%	Clinopyroxene wt.%	Cr-spinel wt.%
SiO_2	36.47	41.14	54.50	
TiO_2	0.05		0.10	0.16
Al_2O_3	0.20		3.05	25.12
Cr_2O_3	0.17	0.03	2.71	40.79
FeO	7.27	8.03	1.72	22.77
MnO	0.07	0.09	0.06	0.36
MgO	42.10	50.42	15.11	11.26
NiO	0.19	0.35	0.04	0.09
CaO	0.19	0.02	19.57	
Na_2O	000		2.79	
H_2O	12.57			
CO_2	0.95			
Total	100.23	100.08	99.65	100.55

EMPA measurements of mineral compositon made by Troneva M.; the bulk composition of the rock 9206 is given by Ukhanov *et al*., (1988)

TABLE 2. OH bands observed in IR spectra of olivines (cm^{-1}).

1	2	3	4
	3215		
		3230	
3331			3334,3327
	3341		
3357			
	3404	3400	
3452		3450	
3482	3478		3478
3497			3500
	3514	3509	
3526	3524	3520	
3535	3535		
3546			3550
3569	3570	3570	3572
3580			
3591	3592		
	3598		
3613			3616
3621	3624		3624
	3640		3638
	3647		
3661			3652
3677	3674		3679

1: synthetic olivine (Young *et al*., 1993); 2: scarn (Libowitsky and Beran, 1995); 3: hydrothermally alterated peridotites from Zabargad, Red sea (Beran and Putnis, 1983); 4: olivine from the mantle nodule 9206, pipe Udachnaya-East, Yakutiya (present work)
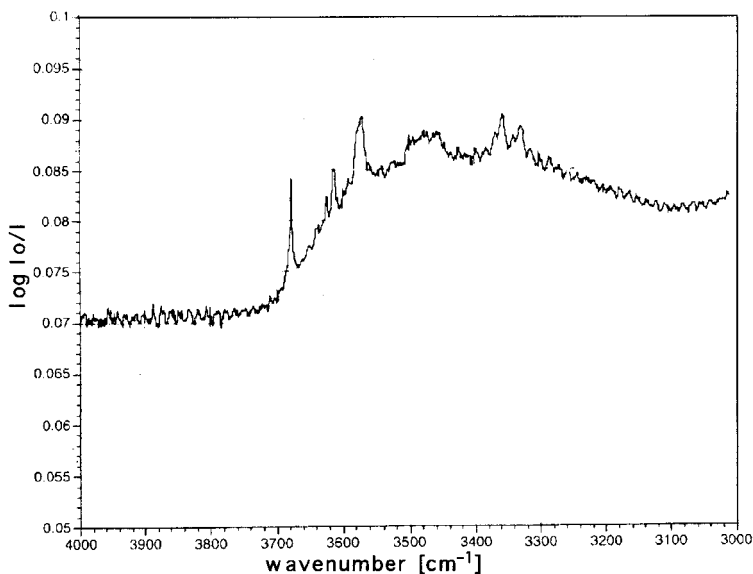
FIG. 2. Unpolarized IR spectrum of the oxidized olivine from the mantle nodule 9206. The observed absorption bands correspond to OH^--groups (c.f. Table 2).

Results

Observations on a macro-scale level

Optical microscopy shows an orange oxidation rim on the (100) plate of the oxidized olivine crystal. The thickness of the rim parallel to (001) is $40-80$ μm, while parallel to (010) the rim is so thin that it cannot be detected by optical microscopy.

Electron microprobe analyses were carried out on different areas of the crystal slab. The chemical composition of the olivine grain is given in Table 1. No variations of Mg and Fe across the crystal, either in the unaffected centre or in the oxidation rim, are observed. There is no change in composition compared with the unoxidized crystal (Table 1). No oxide precipitates are found in the oxidation rim by EMPA.

Polarized UV/vis spectra at a local resolution of 20 μm were obtained separately from the oxidation rim and the centre of the (100) olivine plate (Fig. 1). In the orange rim the spectrum displays broad diffuse shoulders at 19000 and 25000 cm^{-1}, which do not occur in the centre of the crystal (Fig. 1). Such bands indicate the presence of Fe^{3+}-bearing phase(s) in the rim of the (100) olivine plate.

The IR spectrum (Fig. 2) was obtained from the total volume of the crystal in the region of the OH stretching band system consists of seven relative strong bands centred at 3679, 3616, 3572, 3500, 3478, 3450, 3334 and 3327 cm^{-1} (Table 2). Additionally, three weak bands are observed at 3652, 3638 and 3624 cm^{-1}. The band at 3572 cm^{-1} exhibits a shoulder around 3550 cm^{-1}. The FWHM varies between 9 and 13 cm^{-1} for the strong bands. All observed band positions correspond to those reported earlier, which were interpreted as structurally incorporated hydroxyl groups in the olivine structure (Bai and Kohlstedt, 1993; Young et al., 1993; Libowitsky and Beran, 1995).

Observations on the nm-scale

The TEM observations were made near the oxidation rim. The specimen oriented with the [100] zone-axis of olivine parallel to the electron beam, exhibits inclusions with two different morphologies (Fig. 3): (1) Small inclusions ($50-100$ nm in size), almost isometric with very poorly developed crystal faces. Sometimes, a core and rim structure of the inclusions is visible. They show a moiré pattern in the core, whereas no moiré contrast is observed in the narrow rim. Very often the small inclusions are linked to dislocations in the olivine matrix. (2) Large pseudohexagonal
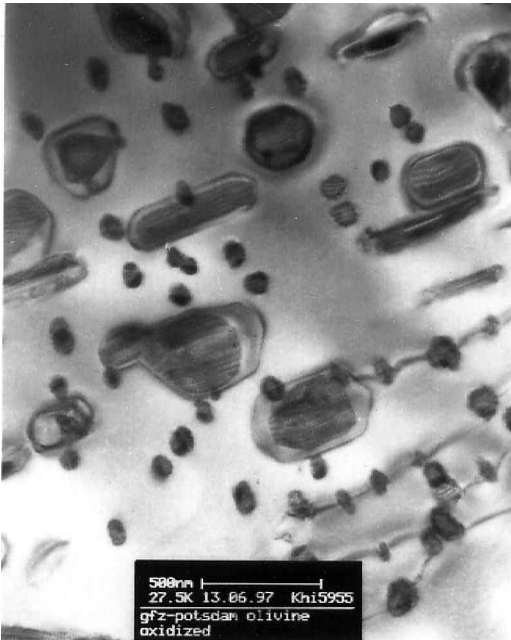
FIG. 3. TEM bright field image of inclusions in the oxidized olivine grain from the mantle nodule 9206.

inclusions with crystal faces, either isometric or elongated (aspect ratio 1–10), are observed. They are not connected to dislocations. The sizes of both the isometric and slightly elongated inclusions (with an aspect ratio up to 1–2) are in the range of 250–600 nm. The inclusions with maximum elongation have a length up to 1500 nm. They are oriented and elongated parallel to the [001] direction of the olivine matrix (Fig. 3). Within the (100) foil of the specimen the crystal faces of the inclusions are parallel to the [001], [01$\bar{1}$] and [011] directions of the olivine matrix. All inclusions exhibit a core and rim structure. Elongated inclusions with an aspect ratio 1–2 show a core which is characterized by a moiré pattern. The core/rim boundaries are parallel to the [010], [012], [01$\bar{2}$] and [001] directions of the olivine matrix.

The orientation of the moiré fringes in all inclusions, both small and large, is always parallel to one another even though they rotate relative to the edges of the crystals when the specimen is tilted. This observation, as well as the electron diffraction and lattice fringe images confirm that the inclusions are crystalline. Lattice fringe images of the phase boundaries olivine/inclusion show only slight distortion of the fringes in the boundary. From the lattice fringe images it is concluded that the inclusions are coherent or semicoherent with the olivine matrix; the d-spacing and the orientation of the lattice fringes in the inclusions correspond to d_{001} and d_{020} of the olivine matrix.

The chemical composition of ten different inclusions of type (1) and (2), the latter with elongation up to 1–2, has been determined by AEM; several analyses from different areas of the same inclusion have been carried out. The results are plotted in Fig. 4. Further, the data show that the inclusions contain only Mg, Fe and Si as cations and that they are enriched in iron compared with the olivine matrix (Fig. 4). The analyses show chemical heterogeneity of the inclusions. They are composed of a core which is enriched in Fe and depleted in Mg compared with the olivine matrix, and a rim of almost the same composition as the olivine matrix. The core which exhibits the moiré contrast, shows a variation of the Si/(Si+Mg+Fe) ratio larger than the experimental error, while the averaged ratios from all measurements are like that of olivine within AEM error (Table 3).

The EELS measurements of the oxygen K-edge region exhibit a pre-peak at ~528 eV in inclusions of both types, (1) and (2), while in EELS spectra of the olivine matrix this pre-peak is absent (Fig. 5). The peak-height ratio of the pre-peak at 528 eV and the maximum intensity of the oxygen K-edge in the near-edge region is higher in the core than in the rim of inclusions and increases with Fe-concentration. According to Wirth (1997), such a pre-peak is related to OH$^-$, whereas van Aken *et al.* (1998) assign it to Fe^{3+} and/or other 3-d transition metals.

Electron diffraction data

Selected area electron diffraction (SAED) and convergent beam electron diffraction (CBED) were used to identify the phases comprising the

TABLE 3. Average Si/(Si+Mg+Fe) ratios.

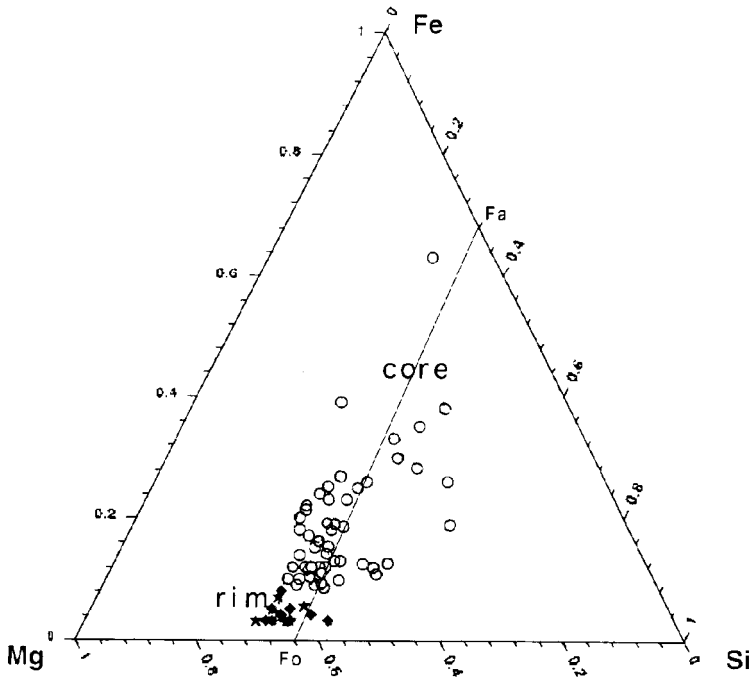| Ratio	Inclusions	Olivine (ideal)
Si/(Si+Mg+Fe)	0.25–0.60	0.33
Fe/(Fe+Mg+Si)	0.05–0.60	0.00–0.67
Mg/(Mg+Fe+Si)	0.10–0.70	0.00–0. 67

FIG. 4. Chemical composition of inclusions (AEM data, minimum error 13% rel.); diamonds – rim of inclusions, open circles – core of inclusions, stars – olivine matrix.
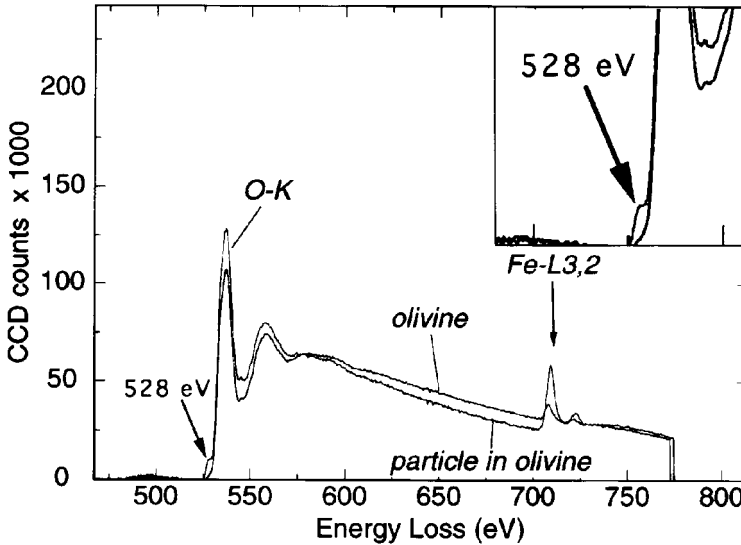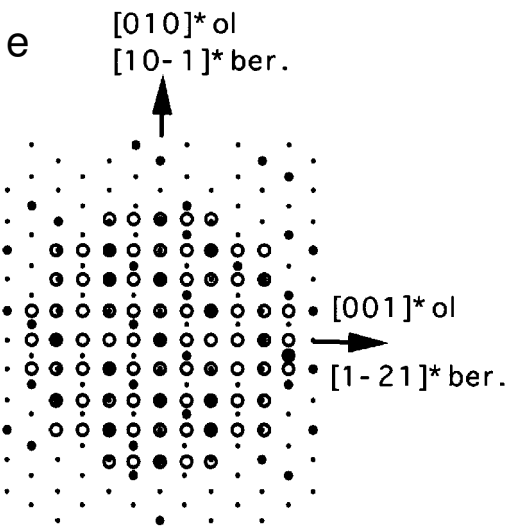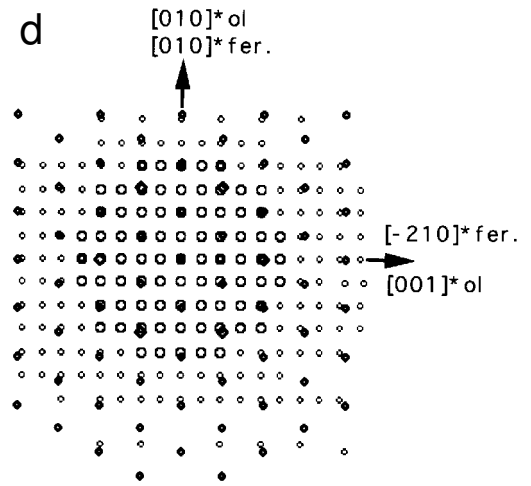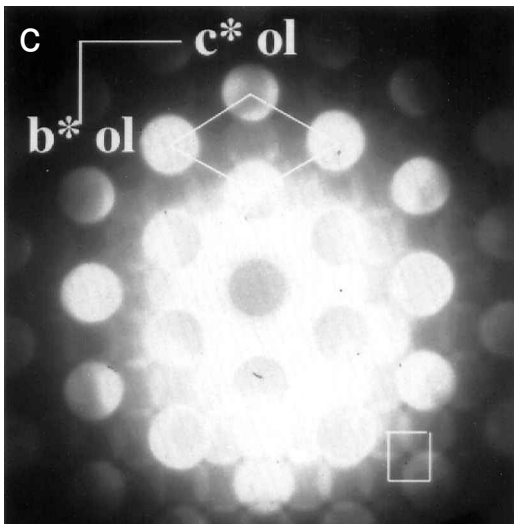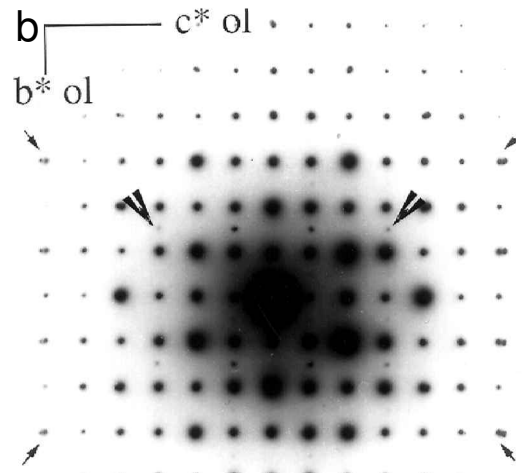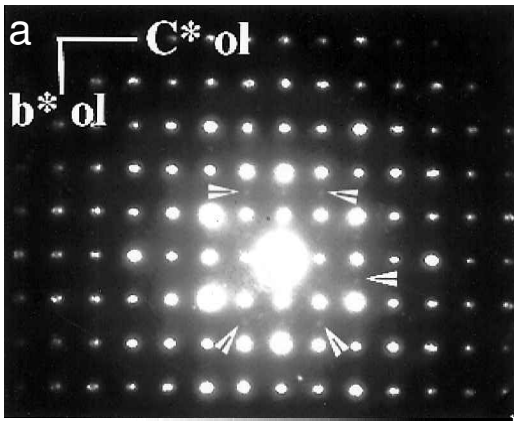

FIG. 5. EEL spectra of inclusion and olivine matrix. A pre-peak at 528 eV in the spectrum of the inclusion is indicated by an arrow. The inserted image shows a magnification of the pre-peak prior to the onset of the oxygen K-edge (O-K). The spectrum of the inclusion shows higher intensities of the Fe L3,2-edges than that of olivine.

inclusions. The size of the largest inclusion is smaller than the area which can be selected by the smallest aperture. Therefore, any observed SAED pattern is composed of diffraction spots from the inclusion and the surrounding matrix. The observed heterogeneity in chemical composition of the inclusions (Fig. 4) suggests that they should be composed of more than one phase. In that case, any SAED pattern obtained from an inclusion represents a superposition of diffraction spots from all its constituent phases and the olivine matrix. The CBED was used to get diffraction data from the inclusions only. Experimental and simulated diffraction patterns are shown in Fig. 6a−e, Fig. 7 and Fig. 8a−d. The SAED and CBED patterns of the inclusions were recorded in three different orientations with the [100] (Fig. 6a−c), [3$\bar{1}\bar{1}$] (Fig. 7) and [$\bar{2}$11] (Fig. 8a,b) olivine zone axes parallel to the electron beam. This was performed by tilting the (100) olivine foil around [01$\bar{1}$]* at ~33−39° and 52−55° respectively. Both the SAED and CBED patterns show three systems of spots in addition to those of the olivine matrix suggesting that the inclusions are composed of phases with three different unit cell geometries: orthogonal (Table 4), hexagonal or trigonal (Table 5) and cubic or pseudocubic (Table 6). In this context the term orthogonal lattice refers to a lattice with at least one 90° angle (it can be anything except triclinic). In the [100] SAED patterns of different inclusions the relative intensities of diffraction spots of these three phases vary: [100] SAED patterns show intense spots from the orthorhombic lattice if the rim of inclusion is well pronounced (Fig. 6a) whereas intense spots of both hexagonal and cubic (or pseudocubic) lattices are observed if the inclusion is significantly enriched in iron (Fig. 6b).
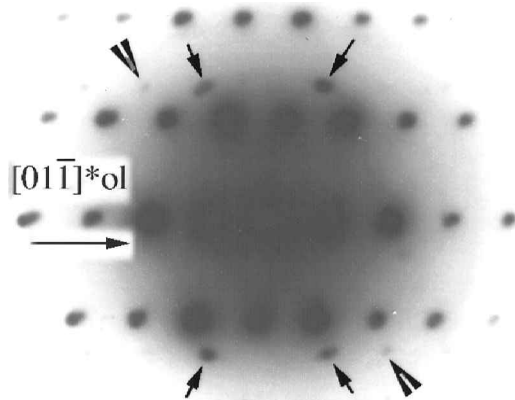

FIG. 7. SAED image of an inclusion with the [3$\bar{1}\bar{1}$] zone axis of olivine parallel to the beam. A superposition of (3$\bar{1}\bar{1}$)*ol//($\bar{4}$11)*cub//(01$\bar{1}$)*hex is observed. Spots of the hexagonal or trigonal phase (small arrows) and the cubic or pseudocubic phase (large arrows) are indicated.

An orthorhogonal lattice with unit cell dimensions of 5.80(10) and 5.25(3) Å is observed in the [100] SAED patterns (Fig. 6a) as an elongation and even a splitting of the olivine diffraction spots along approximately the [001]* direction. Additionally, weak spots are observed with k = 2n+1 which are forbidden in the space group of olivine (*Pbnm*) and are not observed in the SAED patterns of the olivine matrix. The observed unit cell dimensions 5.80 (10) and 5.25 (3) correspond to the unit cell parameters b and c of olivine, and later (see Discussion) the orthorhogonal lattice is interpreted as 'secondary olivine' [100]. The CBED patterns obtained seperately from the rim and the core of the inclusion indicate that the

---

FIG. 6. Experimental (*a*), (*b*), (*c*) and simulated (*d*), (*e*) diffraction patterns of inclusions with the [100] zone axis of the olivine matrix parallel to the beam. (*a*) SAED pattern of an inclusion with a well pronounced rim. Splitting of the olivine spots as well as the presence of weak spots (indicated by arrows) usually forbidden in olivine space group *Pbnm*, are observed. The pattern shows a superposition of the two orthogonal lattices. (*b*) SAED pattern of an inclusion with high content of Fe. A superposition of the (100)* plane of olivine, the (001)* plane of the hexagonal or trigonal phase and the (111)* plane of a cubic or pseudocubic phase is observed (cf. text). The large arrows indicate spots of the cubic or pseudocubic lattice (d = 5.25(10) Å), and the small arrows indicate splitting of spots of the olivine and of the hexagonal (or trigonal) phase with d = 2.54(3) Å. (*c*) CBED pattern of the core of an inclusion with [100] zone axis of olivine parallel to the beam. It shows a superposition of the olivine spots and reflections of the hexagonal or trigonal phase with d = 2.50 Å. Reciprocal lattices of the hexagonal or trigonal phase and olivine are labelled in the upper and lower parts of the image respectively. (*d,e*) Simulated superimposed diffraction patterns of olivine, bernalite and feroxyhite lattices with the [100] zone axis of olivine parallel to the beam. The spots forbidden in the *P$\bar{3}$m*1 (feroxyhite) and *Immm* (bernalite) space groups are included in the simulation. (*d*) A superposition of the (100)*ol // [001]*fer; (*e*) superimposed (100)*ol and (111)*ber. Open symbols – olivine, closed symbols – feroxyhite (*d*) and bernalite (*e*).
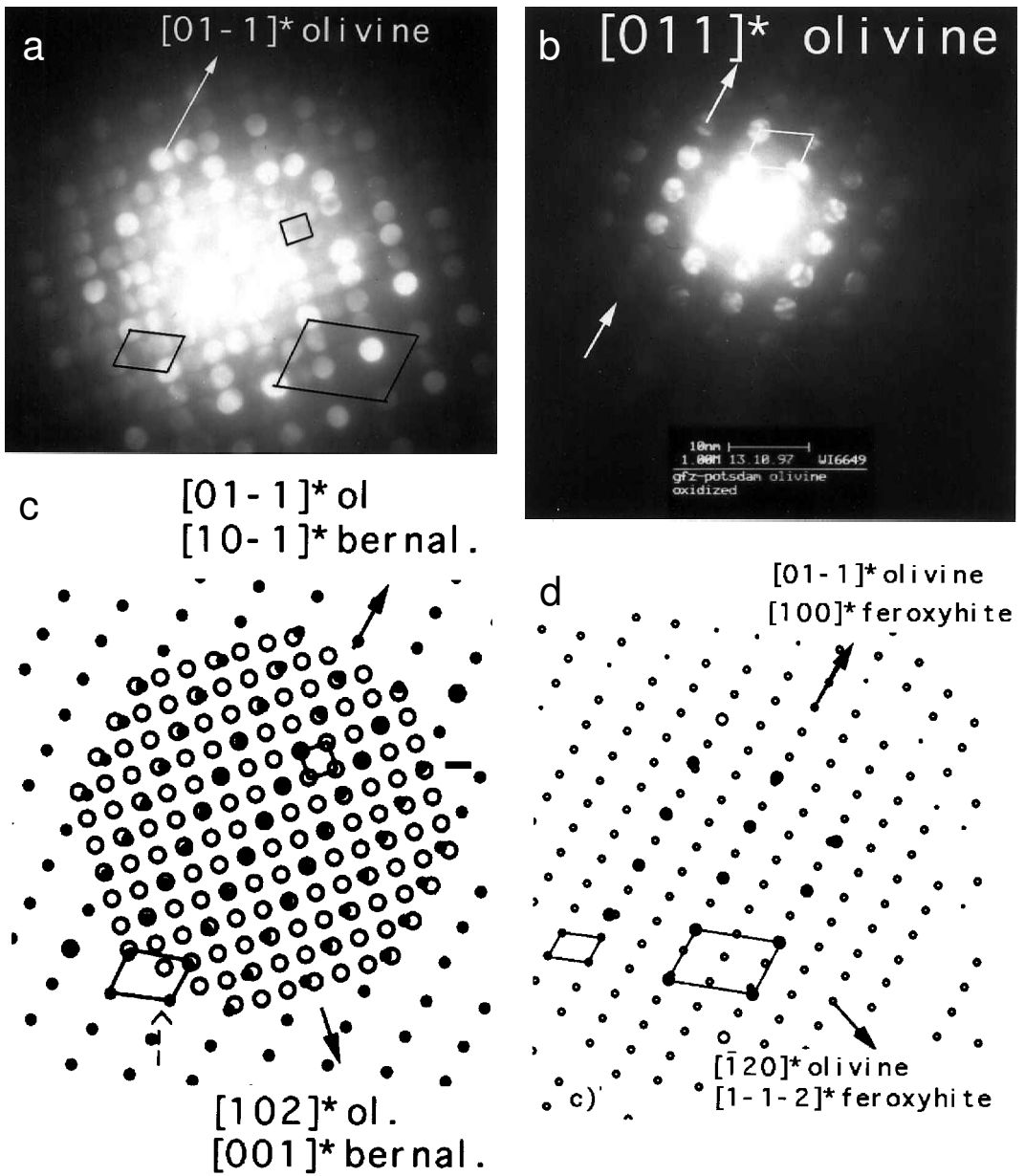
Fig. 8. Experimental (*a, b*) and simulated (*c*), (*d*) electron diffraction patterns of inclusion with the $[\bar{2}11]$ zone axis of olivine parallel to the beam. (*a*) CBED image of the core of an inclusion shows a superposition of $(\bar{2}11)*ol$ // $(010)*cub$ // $(0\bar{2}1)*hex$. Reciprocal lattices of olivine (lower left), of the cubic or pseudocubic phase (lower right) and the hexagonal or trigonal phase (upper right) are labelled. (*b*) CBED pattern of the rim of an inclusion exhibiting olivine diffraction spots only. (*c,d*) Simulated diffraction patterns of lattices of bernalite, feroxyhite and olivine, with $[\bar{2}11]ol$ // $[010]$bernalite // $[0\bar{2}1]$bernalite. The spots forbidden in the $P\bar{3}m1$ (feroxyhite) and *Immm* (bernalite) space groups are included in the simulation. (*c*) Superimposed $(\bar{2}11)*ol$ and $(010)*bernalite$; (*d*) superimposed $(\bar{2}11)*ol$ and $(0\bar{2}1)*feroxyhite$. Small circles – olivine, large open circles – bernalite (*c*), large closed circles – feroxyhite (*d*).

328

TABLE 4. Unit cell parameters and d-dimensions of the orthogonal phase in the rims of inclusions (electron diffraction data)

| | Experimental data | | | | Literature data | | |
| | Matrix (olivine) | | Rim of inclusion | | Olivine Fo$_{96}$ (Eliseev, 1957) | | |
hkl	d_{hkl} (Å)	Unit cell parameters	d_{hkl} (Å)	Unit cell parameters	hkl	d_{hkl} (Å)	Unit cell parameters
001	6.12(3)	a = 4.80(6) Å	5.80(3)		001	6.085	a = 4.812 Å
022	2.62(3)	b = 10.60(5) Å	2.54(3)	b = 10.50(5) Å	022	2.636	b = 10.565 Å
020	5.30(3)	c = 6.12(3) Å	5.25(3)	c = 5.80(3) Å	020	5.282	c = 6.085 Å
111	3.56(10)	α = 90°			111	3.554	α = 90°
120	3.56(10)	β = 90°			120	3.557	β = 90°
102	2.51(10)	γ = 90°			102	2.572	γ = 90°
112	2.52(4)				112	2.498	
121	3.08(4)				121	3.071	
131	2.50(10)				131	2.575	
130	2.84(4)				130	2.842	

doubled olivine spots which characterize the orthogonal lattice are present in the rim pattern. They are not observed in the core pattern.

Hexagonal (trigonal) lattice

A hexagonal net of reflections corresponding to d = 2.54 Å observed at the SAED patterns with the [100] zone axis of olivine parallel to the beam (Fig. 6b) is indexed as (100)* reciprocal lattice plane of a hexagonal (or trigonal) phase. The

corresponding unit cell parameter a_o is 2.93(3) Å. Tilting the specimen with the [$3\bar{1}\bar{1}$] zone axis of olivine parallel to the beam results in a diffraction pattern (Fig. 7) with a net of reflections with d = 2.54(3) and 2.18(4) Å. Relating these reflections to a hexagonal or trigonal phase, the pattern is indexed as ($0k\bar{1}$)* where k = n and $n \neq 0$. The unit cell parameter c_o is determined as c = n*4.40(20) Å. The spots of this hexagonal or trigonal lattice with d = 2.50 Å are observed in [100] CBED patterns of the cores of inclusions

TABLE 5. Unit cell parameters and d-dimensions of the hexagonal or trigonal phase in the cores of inclusions (electron diffraction data).

| Experimental data | | | | | | | | | | | |
| | | FeOOH feroxyhite (Bernal et al., 1959) | | | Mg(OH)$_2$ brucite (Strunz, 1970) | | | Mg$_{2.08}$Si$_{1.16}$H$_{3.20}$O$_6$ Phase E (Kudoh et al., 1993) | | |
d_{hkl} (Å)	Unit cell parameters	hkl	d_{hkl} (Å)	Unit cell parameters	hkl	d_{hkl} (Å)	Unit cell parameters	hkl	d_{hkl} (Å)	Unit cell parameters
2.54(3)	a = 2.93(3) Å	100	2.546	a = 2.941 Å	100	2.721	a = 3.14Å	100	2.56	a = 2.97 Å
2.54(3)	b = 2.93(3) Å	010	2.546	b = 2.941 Å	010	2.721	b = 3.14Å	010	2.56	b = 2.97 Å
1.47(3)	c = 4.40(20)Å	110	1.470	c = 4.49 Å	110	1.571	c = 4.77Å	110	1.48	c = 13.88 Å
2.54(3)	α = 90°	$\bar{1}10$	2.546	α = 90°	$\bar{1}10$	2.721	α = 90°	$\bar{1}10$	2.56	α = 90°
2.18(3)	β = 90°	011	2.210	β = 90°	011	2.363	β = 90°	013	2.24	β = 90°
2.18(3)	γ = 120°	$\bar{1}11$	2.210	γ = 120°	$\bar{1}11$	2.363	γ = 120°	$\bar{1}13$	2.24	γ = 120°
1.66(4)		012	1.660		012	1.793		016	1.72	

TABLE 6. Unit cell parameters and *d*-dimensions of the cubic or pseudocubic phase in the cores of inclusions (electron diffraction data)

Experimental data			Literature data					
			SiO_2 -cristobalite (Heaney, 1994)			Fe(OH)$_3$ bernalite (Birch *et al.*, 1992)		
d_{hkl} (Å)	Unit cell parameters	*hkl*	d_{hkl}(Å)	Unit cell parameters	*hkl*	d_{hkl}(Å)	Unit cell parameters	
5.25(10)	a = 7.40(20) Å	110	5.04	a = 7.13 Å	110	5.34	a = 7.544 Å	
7.40(20)	b = 7.40(20) Å	100	7.13	b = 7.13 Å	100	7.54	b = 7.560 Å	
7.40(20)	c = 7.40(20) Å	010	7.13	c = 7.13 Å	010	7.56	c = 7.558 Å	
5.25(10)	α = 90°	011	5.04	α = 90°	011	5.34	α = 90°	
3.00(5)	β = 90°	121	2.91	β = 90°	121	3.08	β = 90°	
2.18(4)	γ = 90°	113	2.15	γ = 90°	113	2.28	γ = 90°	

(Fig. 6*c*). This phase with unit cell parameters $a = b = 2.93$ Å and $c = n4.40$ Å can be related to brucite $Mg(OH)_2$ ($a = b = 3.12$ Å, $c = 4.73$ Å, $\gamma = 120°$), or feroxyhite FeOOH ($a = b = 2.941$ Å, $c = 4.49$ Å, $\gamma = 120°$, Bernal *et al.*, 1959; Dasgupta, 1961; Drits *et al.*, 1993), or Phase E $Mg_{2.08}Si_{1.16}H_{3.20}O_6$ ($a = b = 2.97$ Å, $c = 13.882$ Å, $\gamma = 120°$, Kudoh *et al.*, 1993, Table 5) Simulated diffraction patterns of superimposed olivine and feroxyhite shown in Fig. 6*c* and Fig. 8*c* are in a good agreement with experimental patterns in Fig. 6*b* and Fig. 8*a*.

Cubic (or pseudocubic) lattice

Additional to the olivine spots in the electron diffraction patterns of the [100] (Fig. 6*b*) and [$\bar{2}$11] (Fig. 8*a*) zone axis of olivine there are reflections which form a hexagonal net with $d = 5.25(10)$ Å and a tetragonal net with $d = 7.40$ Å respectively. These nets are indexed respectively as (111)* and (100)* reciprocal lattice planes of a cubic (or pseudocubic) phase with unit cell parameter $a = 7.40$ Å. Such a unit cell with $a = 7.40(20)$ Å can be referred (Table 6) to as bernalite Fe(OH)$_3$ ($a = 7.544$ Å, $b = 7.560$ Å, $c = 7.558$ Å, space group *Immm* (Birch *et al.*, 1993; McCammon *et al.*, 1995)) or β-cristobalite SiO_2 ($a = b = c = 7.13$ Å, space group $Fd3m$ (Heaney, 1994)). Simulated diffraction patterns of superimposed olivine and bernalite (Fig. 6*e*, Fig. 8*c*) are in good agreement with the corresponding experimental patterns.

The CBED patterns show that both hexagonal or trigonal and cubic or pseudocubic lattices specify the core of inclusions (Figs. 6*c*, 8*a*) and are not observed in the rim (Fig. 8*b*).

Orientation relationship of the phases

The following superposition of reciprocal lattices of the olivine (ol), hexagonal or trigonal (hex) and cubic or pseudocubic (cub) phases are observed in SAED patterns:

$(100)^*_{ol}$ // $(001)^*_{hex}$ // $(111)^*_{cub}$
$(3\bar{1}\bar{1})^*_{ol}$ // $(01\bar{1})^*_{hex}$ // $(\bar{4}11)_{cub}$
$(\bar{2}11)^*_{ol}$ // $(0\bar{2}1)^*_{hex}$ // $(100)^*_{cub}$

The following orientation relationship between lattices are observed:

$[100]_{ol}$ // $[100]_{hex}$, with $[100]_{ol} \wedge [111]_{cub} = 3°$
$[\bar{2}11]_{ol}$ // $[100]_{cub}$, with $[\bar{2}11]_{ol} \wedge [0\bar{2}1]_{hex} = 4°$
$[01\bar{1}]_{hex}$ // $[\bar{4}11]_{cub}$, with $[3\bar{1}\bar{1}]_{ol} \wedge [01\bar{1}]_{hex} = 6°$

$[010]_{ol}$ // $[\bar{1}10]_{hex}$ // $[10\bar{1}]_{cub}$
$[01\bar{1}]_{ol}$ // $[100]_{hex}$ // $[01\bar{1}]_{cub}$
$[001]_{ol}$ // $[[100]_{hex}$ // $[[1\bar{2}1]_{cub}$

the angular relationship of the lattices is given in Table 7.

Discussion

Chemical composition of inclusions

The AEM data show variations of Mg, Fe and Si content inside the inclusions (Fig. 4). Additionally, the data show that the iron content is significantly higher in the core of inclusions compared to the matrix, and that the average Si/((Mg+Fe+Si) ratio is ~0.30, close to that of olivine within the error of AEM. The wide variation of Mg/Fe may be caused by a variable effective thickness of an Fe-rich inclusion which is obviously smaller than the total thickness of the foil. Because the volume fractions of iron-rich

TABLE 7. Angles of tilting, observed zone axis and calculated angles between the zone axis.

Tilt angle	Observed zone axis	Calculated angles
$0-3°$	$[100]_{ol} \mathbin{//} [001]_{hex} \mathbin{//} [111]_{cub}$	$[100]_{ol} \wedge [001]_{hex} \wedge [111]_{cub} = 0°$
$33-39°$	$[3\bar{1}\bar{1}]_{ol} \mathbin{//} [01\bar{1}]_{hex} \mathbin{//} [\bar{4}11]_{cub}$	
		$[100]_{ol} \wedge [3\bar{1}\bar{1}]_{ol} = 39°$
		$[001]_{hex} \wedge [01\bar{1}]_{hex} = 33°$
		$[111]_{cub} \wedge [\bar{4}11]_{cub} = 35°$
$52-55°$	$[\bar{2}11]_{ol} \mathbin{//} [02\bar{1}]_{hex} \mathbin{//} [100]_{cub}$	$[100]_{ol} \wedge [\bar{2}11]_{ol} = 52°$
		$[111]_{cub} \wedge [100]_{cub} = 55°$
		$[001]_{hex} \wedge [02\bar{1}]_{hex} = 48°$

inclusion and the Mg-rich matrix penetrated by the beam may vary, the Fe/Mg ratio will also vary, even if the analysed area is very small.

The EELS results indicate the presence of either Fe^{3+} or OH^- or both of them in the inclusions. The presence of Fe^{3+} in the oxidized rim of the olivine grain is also confirmed by absorption spectroscopy (Fig. 1). The IR spectroscopy shows the presence of OH^- in the crystal plate; the bands observed resemble those in other olivines (Table 2). The bulk composition of an inclusion can be reconstructed from the AEM and EELS data resulting in a Mg hydrous silicate enriched in iron relative to the olivine matrix. Assuming a precursor inclusion phase existed which transformed later into the rim and the core during the heating experiment, the bulk composition of the inclusions represents the composition of a precursor phase. A precursor iron-rich phase could have been formed in the early stage of inclusion generation o, or it could have been created as an iron-depleted phase which subsequently enriched in iron by diffusion of Fe from the olivine matrix during the oxidation process.

Phase composition of inclusions

Electron diffraction data show that the rims of inclusions consist of an orthorhombic phase (Table 4), whereas the cores are composed of a mixture of the hexagonal or trigonal phase and the cubic or pseudocubic phase (Tables 5 and 6). The diffraction patterns of the hexagonal or trigonal phase can be interpreted as either brucite, or feroxyhite, or Phase E (Table 5), while the cubic or pseudocubic phase may be interpreted as β-cristobalite and/or bernalite (Table 6). The AEM

data must be considered in order to identify the constituent phases.

The rim of inclusions

The chemical composition of the rim is similar to that of the matrix. Thus, electron diffraction data (Table 4) as well as AEM measurements (Fig. 4) indicate that the rims of inclusions consist of olivine which deviates slightly in composition with respect to the olivine matrix. This phase is, hereafter termed 'secondary olivine'. The unit cell parameters $b_0 = 10.50(5)$ Å and $c_0 = 5.80(4)$ Å of the 'secondary olivine' are smaller than those of the olivine matrix ($b_0 = 10.60(5)$ Å, $c_0 = 6.12(3)$ Å, Table 4). This could mean that the 'secondary' olivine is either more magnesian-rich than the olivine matrix or it is compressed along the [100] direction. A similar structural compression was described for an olivine containing nm-scale precipitates of magnesioferrite (Khisina *et al.*, 1995). Weak diffraction spots with $k = 2n+1$, forbidden in the *Pbnm* space group of olivine and observed in the (100)* SAED patterns of inclusions (Fig. 7a), can result from a double-diffraction indicating that either the 'secondary olivine' in the rim of the inclusions or underlying olivine matrix or both are very thin along the [100] direction. No forbidden spots are observed in the SAED pattern of the olivine matrix adjacent to the inclusions. Assuming the same specimen thickness in the olivine matrix and the adjacent inclusions, dynamic diffraction causing the forbidden spots can be excluded in that case.

The core of inclusions

The MgO content of the core equals that of the matrix (Fig. 4). This excludes the presence of

brucite in the core. The cores of inclusions are enriched in iron (Fig. 4) and the pre-peak in the EELS spectra indicates the presence of Fe^{3+} or OH^- or both. Thus, feroxyhite is the preferential candidate to explain the hexagonal or trigonal phase. On the other hand, diffraction data obtained are so close to those of Phase E (Table 4) that Phase E cannot be ruled out with certainty, and may be present as a relic of a precursor phase. The cubic or pseudocubic phase may be assigned to bernalite by the same arguments.

Feroxyhite FeOOH and bernalite $Fe(OH)_3$ require the presence of a SiO_2-rich phase, to keep the $(Mg+Fe)/Si$ ratio of the bulk of the inclusion core close to that of olivine (Fig. 4, line Fo-Fa). Such Si-rich phase(s) in the core can be either pyroxene or a SiO_2 phase. We found no indication of pyroxene whereas a cubic or pseudocubic phase may be related to β-cristobalite (Table 6). Experimental data (Tables 5 and 6) are inconsistent with other known iron oxides, iron hydroxides and hydrosilicates except those given in the tables. This means that the cubic or pseudocubic phase is assigned to a mixture of bernalite $Fe(OH)_3$ and β-cristobalite, which can not be discriminated in their diffraction patterns within the experimental error.

The results are interpreted as overlapping feroxyhite, β-cristobalite, and bernalite layers alternating along the [100] direction of the olivine matrix, would explain the observed moiré contrast in the core of inclusions (Fig. 3). The (001) layers of feroxyhite and (111) layers of bernalite and β-cristobalite have a similar geometry and are overlapped with a misfit angle of 3° between the hexagonal and cubic lattices, thus creating a moiré contrast. Close orientation relationship and closely matching unit cell dimensions yield coherency between the phases inside the inclusions. Vertical heterogeneity of the layered inclusions as well as their variable thickness with respect to the foil thickness results in the variation in the Fe/Si as well as the Mg/(Mg+Fe+Si) ratio. The layered microstructure and variable thickness of the inclusions in the foil as well as their probable zoned structure seem to be a reason for the variable relative intensities of diffraction spots from coexisting phases observed in diffraction patterns from different inclusions.

lite and the rim is formed of olivine. The assemblage feroxyhite+bernalite+β-cristobalite is metastable under the conditions of our heating experiment in air at 700°C, 1 atm. The thermodynamically stable products of olivine under oxidizing conditions are magnetite, hematite and quartz. Heating olivine powder under the same P-T-P_{O_2}-time conditions would have resulted in the formation of laihunite or laihunite + magnesioferrite + quartz for increased heating time (Khisina *et al.*, 1995). We conclude that the mechanisms of olivine oxidation under 'dry' and 'wet' conditions as well as in powder and coarse grained samples are different. When olivine is 'wet', then iron hydroxides instead of iron oxides are exsolved during oxidation. This conclusion is supported by a recent Mössbauer spectroscopy study of majorite and wadsleiite (McCammon *et al.*, 1999) showing that $Fe^{3+}/\Sigma\bar{F}e$ is much higher in hydrous phases than in the 'dry' phases.

The phase assemblage feroxyhite + bernalite + β-cristobalite is thermodynamically forbidden at the P_{O_2}-T conditions of the experiment (700°C in air). Both feroxyhite and bernalite should have lost water and transform to hematite at temperatures greater than $100-200°C$ (Birch *et al.*, 1992, 1993; Bernal *et al.*, 1959; Dasgupta, 1961). β-cristobalite is a high-temperature form of SiO_2 thermodynamically stable at temperatures greater than 1470°C (Heaney, 1994); at temperatures <870°C β-quartz as a polymorph of SiO_2 is stable (Heaney, 1994). However, metastable nm-sized precipitation of cristobalite or tridymite, instead of the thermodynamically stable quartz is a ubiquitous phenomenon and was observed previously in oxidized olivine by Champness (1970) and Kohlstedt and Vander Sande (1975). FeOOH, $Fe(OH)_3$ and β-cristobalite which are not equilibrium phases can be stabilized by the effect of "forced equilibria" (Urusov *et al.*, 1997) which shifts the equilibrium reaction by a strain energy term resulting from coherent interfaces. Moreover, nm-scale precipitates encapsulated in the host mineral are constrained by its crystal structure; that is also a factor of 'forced equilibrium' (Urusov *et al.*, 1997).

It is concluded that the thermodynamics of macroscopic phase equilibria may be questioned for nm-scale phase assemblages.

Phase equilibria at the nm scale

The results indicate that the core of inclusions is composed of feroxyhite, bernalite and β-cristoba-

Speculations about the origin of inclusions

The origin and microstructure of the inclusions which are observed in the olivine grain from

mantle nodule 9206 have to be discussed together with the geological setting and the experimental treatment of the crystal: (1) original crystallization or recrystallization of the mineral; (2) serpentinization of olivine and other metasomatic processes and (3) heating under laboratory conditions. The complex microstructure of the inclusions can be considered as a result of a transformation of a precursor phase. Transformation is suggested to proceed during the oxidation experiment and the iron diffusion from the olivine matrix to the inclusions should be involved in this process. The chemical data (Fig. 4) suggest that the precursor phase of the inclusions may be a hydrous magnesian silicate (HMS). The Si/Si+Mg+Fe ratio of these inclusions (~0.30) is close to that of olivine (0.33) and Phase E ($0.317-0.357$). Moreover, the unit cell geometries of Phase E, as a possible precursor phase, and feroxyhite, as a product of its transformation, are very similar and they both are in good agreement with the electron diffraction data (Table 5). These arguments do not, therefore, exclude Phase E as a precursor phase. Another explanation of the observed microstructure of the inclusions can be that the inclusions were exsolved from the olivine matrix during the experimental heating and oxidation. In this case, the inclusions could be nucleated as multi-phase precipitates by interaction of OH^-- and Fe^{3+}-bearing point defects in the olivine matrix. The main question arising from our observations is whether a precursor phase of the inclusions ever existed and what the precursor phase was. To elucidate the origin of inclusions we need to investigate unoxidized olivine grains from both the 9206 and other mantle nodules in kimberlites. This work is in progress.

Conclusions

Experimentally oxidized olivine from a mantle nodule in kimberlite (Udachnaya pipe, Siberia) contains OH^--, Fe^{3+}-bearing crystalline inclusions. The microstructure of inclusions is characterized by a core composed of coexisting feroxyhite FeOOH, bernalite $Fe(OH)_3$ and β-cristobalite SiO_2 with a rim composed of a 'secondary olivine'. It is suggested that this complex microstructure is the result of a solid state transformation of a precursor phase, or may be a hydrous magnesian silicate, occurring on experimental heating and oxidation of the host olivine grain.

Neither laihunite nor magnetite and hematite precipitates were observed as oxidation products within the olivine matrix, whereas Fe^{3+}-hydroxides were found in the core of inclusions. This result provides evidence that the mechanisms of olivine oxidation under 'dry' and 'wet' conditions as well as in powder and coarse grained samples are different; when olivine contains either OH-bearing point defects or inclusions of OH-bearing phases then iron hydroxides instead of iron oxides are exsolved during the oxidation.

The IR spectrum of the oxidized olivine grain contains the same absorption bands as those of unoxidized olivine samples. The latter are usually interpreted as OH-bearing point defects incorporated in the olivine structure. Infrared spectra of iron hydroxides are different from those observed in this study. Data from the literature show that the IR spectrum of bernalite does not contain absorption bands in the $3200-3600$ cm^{-1} region (McCammon *et al.*, 1995). This means that feroxyhite and bernalite which are found in the cores of inclusions cannot produce the observed absorption bands. Taking into account that the IR spectrum is obtained from the whole volume of the sample whereas the Fe^{3+}, OH-bearing, inclusions occur only in the very thin oxidation rim, we can assume that the major contribution to the IR spectrum comes from the unoxidized interior of the olivine grain. Assuming a hydrous magnesium silicate (HMS) to be the precursor phase of the inclusions we can speculate that unaltered HMS inclusions can contribute to the IR-spectrum. Vibrational frequencies of phase E which is assumed to be a possible precursor phase, were observed at 3642, 3616, 3598, 3368 and 3311 cm^{-1} (Mernagh and Lin-Gun Liu, 1998) and are comparable to those of olivine. Unoxidized samples will be investigated by TEM to solve the problem of the precursor phase and to allow an unambiguous interpretation of IR spectra. This work is in progress. Our results show that the interpretation of IR spectra with respect to the OH occurrence is ambiguous without knowledge of the microstructure.

References

Bai, Q. and Kohlstedt, D.L. (1993) Effects of solubility and incorporation mechanism. *Phys. Chem. Min.*, **19**, 460–71.

Banfield, I.F., Dyar, M.D. and McGuire, A.V. (1992) The defect microstructure of oxidised olivine from Dish Hill, California. *Amer. Mineral.*, **77**, 977–86.

Beran, A. and Putnis, A. (1983) A model of the OH-positions in olivine, derived from infrared spectroscopy investigations. *Phys. Chem. Min.*, **9**, 57–60.

Bernal, J.D., Dasgupta, D.R. and Mackay, A.L. (1959) The oxides and hydroxides of iron and their structural relationships. *Clay Miner. Bull.*, **4**, 15–30.

Birch, W.D., Pring, A., Reller, A. and Schmalle, H. (1992) Bernalite: a new ferric hydroxide with perovskite structure. *Naturwiss.*, **79**, 509–11.

Birch, W.D., Pring, A., Reller, A. and Schmalle, H.W. (1993) Bernalite, Fe(OH)₃, a new mineral from Broken Hill, New South Wales: description and structure. *Amer. Mineral.*, **78**, 827–34.

Burnley, P.C. and Navrotsky, A. (1996) Synthesis of high-pressure hydrous magnesium silicates: observations and analysis. *Amer. Mineral.*, **81**, 317–26.

Champness, P.E. (1970) Nucleation and growth of iron oxides in olivine. *Mineral. Mag.*, **37**, 790–800.

Dasgupta, D.R. (1961) Topotactic transformations in iron oxides and oxyhydroxides. *Ind. J. Physics*, **35**, 401–19.

Drits, V.A., Sakharov, B.A. and Manceau, A. (1993) Structure of ferohyhite as determined by simulation of X-ray diffraction curves. *Clay Miner.,* **28**, 209–22.

Dyar, M.D., Delaney, J.S., Sutton, S.R. and Schaefer, M. (1998) Fe³⁺ distribution in oxidised olivine: a synchrotron micro-XANES study. *Amer. Mineral.* **83**, 1361–5.

Eliseev, E.N. (1957) X-ray study of the minerals of the isomorphous series forsterite-fayalite. *Zap. Vses. Min. Obshch.,* **86**, 657–70 (in Russian).

Freund, F. and Oberheuser, G. (1986) Water dissolved in olivine: a single-crystal infrared study. *J. Geophys. Res.*, **91**, 745–61.

Goldstein, J.I. and Williams, D.B. (1989) Quantitative X-ray analysis. Pp155–218 in: *Principles of Analytical Electron Microscopy* (D.C. Joy, A.D. Romig and J.I Goldstein, editors). Plenum Press, New York.

Griffiths, P.R. and de Hazeth, J.A. (1986) *Fourier Transform Infrared Spectroscopy*. Wiley & Sons, New York.

Heaney, P.E. (1994) Structure and chemistry of the low-pressure silica polymorphs. Pp. 1–40 in: *Silica* (P.E. Heaney, editor). Reviews in Mineralogy, **29**, Mineralogical Society of America, Washington D.C.

Janney, D.E. and Banfield, J.F. (1998) Distribution of cations and vacancies and the structure of defects in oxidised intermediate olivine by atomic-resolution TEM and image simulation. *Amer. Mineral.*, **83**, 799–810.

Khisina, N.R., Khramov, D.A., Kolosov, M.V., Kleschev, A.A. and Taylor, L.A. (1995) Formation of ferriolivine and magnesioferrite from Mg-Fe-olivine: reactions and kinetics of oxidation. *Phys. Chem. Min.*, **22**, 241–50.

Khisina, N.R., Khramov, D.A., Kleschev, A.A. and Langer, K. (1998) Laihunitization as a mechanism of olivine oxidation. *Eur. J. Mineral.*, **10**, 229–38.

Khisina, N.R., Rusakov, V.S. and Kleschev, A.A. (1999) On the PO₂-T conditions of laihunite formation. *Geokhimiya*, **9**, 994–9.

Kitamura, M., Kondoh, S., Morimoto, N., Miller, G.H., Rossman, G.R. and Putnis, A. (1987) Planar OH-bearing defects in mantle olivine. *Nature*, **328**, 143–5.

Kohlstedt, D.L. and Vander Sande, J.B. (1975) An electron microscopy study of naturally occurring oxidation produced precipitates in iron-bearing olivines. *Contrib. Mineral. Petrol.*, **53**, 13–24.

Kudoh, Y., Finger, L.W., Hazen, R.M., Prewitt, C.T., Kanzaki, M. and Veblen, D.R. (1993) Phase E: a high-pressure hydrous silicate with unique crystal chemistry. *Phys. Chem. Min.*, **19**, 357–60.

Laihunite Research Group (1976) Laihunite – a new iron silicate mineral. *Geochimica*, **1976**, 95–103.

Libowitsky, E. and Beran, A. (1995) OH defects in forsterite. *Phys. Chem. Min.*, **22**, 387–92.

Liu, L.-G. (1987) Effects of H₂O on the phase behaviour of the forsterite-enstatite system at high pressures and temperatures and implications for the Earth. *Phys. Earth Planet. Interiors*, **49**, 142–67.

Matzyuk, S.S., Platonov, A.N. and Polshin, E.V. (1989) *Spineloids from Mantle Rocks*. Naukova Dumka, Kiev (in Russian).

McCammon, C.A., Pring, A., Keppler, H. and Sharp, T. (1995) A study of bernalite, Fe(OH)₃, using

Mössbauer spectroscopy, optical spectroscopy and transmission electron microscopy. *Phys. Chem. Min.*, **22**, 11–20.

McCammon, C.A., Smyth, J.R., Laustsen, H.M.S. and Ross, N.L. (1999) Oxidation state of iron in hydrous silicate phases. *J. Conf. Abstr*., **4**, 653.

Mernagh, T.P. and Liu, L.-G. (1998) Raman and infrared spectra of Phase E, a plausible hydrous phase in the mantle. *Canad. Mineral.,* **36**, 1217–23.

Miller, G.H., Rossman, G.R. and Harlow, G.E. (1987) The natural occurrence of hydroxyl in olivine. *Phys. Chem. Min.,* **14**, 461–72.

Prewitt, C.T., Yang, H. and Frost, D.J. (1997) Current status of the DHMS alphabet phases. *EOS*, F729–F730.

Strunz, A. (1970) *Mineralogische Tabellen*. Akademische Verlags gesellschaft Geest & Portig K.-G, Leipzig.

Thompson, A.B. (1992) Water in the Earth's upper mantle. *Nature*, **358,** 295–302.

Ukhanov, A.V., Ryabchikov, I.D. and Kharkiv, A.D. (1988) *Lithospheric Mantle of the Yakutiya Kimberlite Province*. Nauka, Moscow (in Russian).

Urusov, V.S., Tauson, V.L. and Akimov, V.A. (1997) *Solid State Geochemistry*. Moscow, GEOS', 500 pp (in Russian).

van Aken, P.A., Liebscher, B. and Styrsa, V.J. (1998) Core level electron energy loss spectra of minerals: pre-edge fine structures at the oxygen K-edge. *Phys. Chem. Min.*, **25**, 494–8.

Wirth, R. (1997) Water in minerals detectable by electron energy-loss spectroscopy EELS. *Phys. Chem. Min.*, **24**, 561–8.

Young, T.E., Green, H.W. II, Hofmeister, A.M. and Walker, D. (1993) Infrared spectroscopy investigation of hydroxyl in -(Mg,Fe)$_2$SiO$_4$ and coexisting olivine: implications for mantle evolution and dynamics. *Phys. Chem. Min.*, **19**, 409–22.